Unsteady Flow Evolution Through a Turning Midturbine Frame Part 2: Spectral Analysis

D. Lengani,* R. Spataro,† J. Peterleithner,‡ and E. Göttlich§
Graz University of Technology, A-8010 Graz, Austria

DOI: 10.2514/1.B35487

This paper analyzes the propagation of the aerodynamic deterministic stresses through a two-spool counter-rotating transonic turbine at Graz University of Technology. The test setup consists of a high-pressure stage, a diffusing midturbine frame with turning struts and a counter-rotating low-pressure rotor. The discussion of the data is carried out in this second part paper on the basis of spectral analysis. The theoretical framework for a double Fourier decomposition, in time and space, is introduced and discussed. The aim of the paper is the identification of the sources of deterministic stresses that propagate through the turbine. A fast-response aerodynamic pressure probe has been employed to provide time-resolved data downstream of the high-pressure rotor and of the turning strut. The fast-response aerodynamic pressure probe measurements were acquired together with a reference signal (a laser vibrometer) downstream of the high-pressure rotor to identify different sources of deterministic fluctuations. The discussion is completed by fast-response pressure measurements on the strut surface and computational fluid dynamics computation to detail which deterministic stress related to the high-pressure stage propagates through the duct. The double Fourier decomposition shows that structures at the periodicity of the rotor blade number decay, whereas the unsteadiness at the outlet of the duct is the result of vane–rotor–vane interaction.

Nomenclature

A	=	Fourier coefficient of circumferential mode
B	=	number of blades
f	=	frequency
H	=	relative channel height
m	=	circumferential mode
n	=	index of harmonic of blade passing frequency
n_c	=	number of circumferential points
n_t	=	number of points within revolution period
p_s	=	static pressure
p_t	=	total pressure
r	=	radius
t	=	time
V	=	number of vanes
θ	=	circumferential coordinate
Ω	=	rotor angular velocity
$< >$	=	deterministic periodic component

Superscripts

$-$	=	time-averaged properties
$\sim$	=	ensemble-averaged properties
$'$	=	stochastic fluctuating component

I. Introduction

AS DISCUSSED in the companion paper [1], a component that has a critical impact on the overall performance of modern and future generation aeroengines is the diffusing duct, which connects the high-pressure (HP) with the low-pressure (LP) turbine frame. The current state of the art of this component, which is about to enter commercial production within the PW1000G program, is represented by a new concept of integrated design: a large vane installed within the intermediate diffusing duct should merge the mechanical function of a strut (structural components) with the aerodynamic performance of an LP-vane (e.g., [2,3]). In this configuration, the first LP stage is composed of the intermediate turbine diffuser populated with these turning vanes and an LP rotor at the outlet of the duct. Furthermore, to reduce the aerodynamic loading of the large LP vane and to optimize the mechanics of the engine, the HP and LP spools are counter-rotating.

A large number of studies deal with such components, as documented in the review paper of Göttlich [4]. However, as mentioned in part 1 [1], just a small percentage of these present the analysis of unsteady effects on a realistic configuration constituted by a transonic HP stage followed by an intermediate duct. Among these, an even lower fraction (e.g., Davis et al. [5], Haldeman et al. [6], and Lavagnoli et al. [7]) discussed the data in the Fourier domain, taking particular notice of the frequencies propagating through the duct. For example, the analysis of Lavagnoli et al. [7] highlighted that, along the strut surface, the dominant frequency is not always the blade passing frequency, but depending on the flow condition, the harmonics could be the frequencies with the highest amplitude. The knowledge of which frequencies (which periodic excitation) travel through the diffusing duct seems an important requirement for the aeromechanical and aeroacoustic optimization of the LP turbine stages. This is crucial in two-spool counter-rotating configurations where the LP rotor sees the neighboring vanes and the HP rotor as sources of unsteady excitations (see, for example, Praisner et al. [8]).

Recently, an engine-relevant test setup for turning midturbine frames (TMTF) with up- and downstream turbine stages with counter-rotating rotors has been developed at Graz University of Technology. Previously published results from this facility in different configurations (baseline TMTF in Lengani et al. [9] and TMTF with splitter vanes in Spataro et al. [10,11]) have focused their attention on the unsteadiness at the outlet of the LP stage. They have shown that the unsteady pressure perturbation from the upstream HP stage contributes considerably to the overall pressure fluctuations at the exit of the second stage. A nonnegligible contribution to this unsteadiness is generated also by the interactions of the rotors even though there is a diffusing flow between them. Spataro et al. [11] showed that the deterministic stresses due to the HP stage, which propagate through the duct, are damped out by merging the strut with LP vanes in one multisplitter component [10].

Received 12 June 2014; revision received 5 February 2015; accepted for publication 12 May 2015; published online 1 October 2015.

*Institute for Thermal Turbomachinery and Machine Dynamics; currently Dipartimento di Ingegneria Meccanica, Energetica, Gestionale e dei Trasporti, Università di Genova 16146 Genova, Italy; davide.lengani@edu.unige.it.

†Institute for Thermal Turbomachinery and Machine Dynamics; currently Whittle Laboratory, Department of Engineering, University of Cambridge, Cambridge, England CB2 1TN, United Kingdom; rs801@cam.ac.uk.

‡Institute for Thermal Turbomachinery and Machine Dynamics.

§Institute for Thermal Turbomachinery and Machine Dynamics; emil.goettlich@tugraz.at (Corresponding Author).

The present paper extends the analysis proposed by Lengani et al. [9]. The purpose of this two-part paper is a detailed discussion of the unsteady flow propagation within the duct. This is discussed in the first part [1] considering experimental data together with validated computational fluid dynamics (CFD) results and following the temporal and spatial evolution of flow structures from the outlet of the HP rotor to the inlet of the LP rotor. This second part paper analyzes the results of part 1 [1] from the perspective of Fourier analysis. In the frequency domain, it is easy to identify the frequency of an energy peak, hence the frequency at which the deterministic fluctuations occur. Variation of amplitude determines whether the deterministic component is decaying or propagating. It is shown that these are linked to the blade passing frequency (BPF) of the HP rotor. Deterministic fluctuations at unexpected (unrelated to the rotor rotation) frequencies are also observed. To confirm this, a set of complementary measurement techniques are used. Two of them are described in part 1 [1]: the fast-response aerodynamic pressure probes (FRAPP) and the fast-response pressure sensors (Kulite sensor mounted on the strut). This paper introduces the use of a laser vibrometer (LV) in a measurement combined with the FRAPP. The two instruments have been positioned up- and downstream of the strut and acquired data at the same time to allow cross correlation.

This work applies the data analysis method, based on the modal decomposition of Tyler and Sofrin [12], presented in Lengani et al. [13,14] (similar analyses are applied by other authors, e.g., Courtiade et al. [15] and Gougeon and Ngo Boum [16]). Particularly, in the previous contribution of Lengani et al. [13], a double Fourier decomposition in time and space was applied to the unsteady CFD results at the exit of a two-stage turbine. This decomposition simplifies the unsteady data into a superposition of a well-defined and limited number of lobed patterns or spinning modes along the circumferential direction at given frequencies. The analysis of unsteady data in the "spatial mode frequency" domain is the logical extension of the commonly used time to frequency domain transformation. The advantage of this data treatment is the capability of isolating the deterministic stresses due to the rotor from the deterministic stresses due to the vane/blade interaction. It is further used as a CFD validation tool because the overall unsteadiness (its temporal and spatial evolution) is represented by a limited number of well-defined modes, which are easily compared.

The structure of this second part paper is as follows:

1) A theoretical background is provided to make the reader familiar with the double Fourier decomposition. For this purpose, its physical meaning is discussed comparing it with well-known CFD models.

2) The study methodology, facility, CFD, and measurement techniques are briefly reported, because they are described in more detail in part 1 [1]. More details are provided for the laser vibrometer and Fourier decompositions, not discussed in part 1.

3) Results are divided in two main sections: data in the frequency domain of the experimental results are shown in the first section. In the second, the double Fourier decomposition of the CFD data is provided; it is validated in comparison with FRAPP data and then its results are discussed.

II. Theoretical Background

A. Periodical Flows, Decomposition

A classical, largely used method for the analysis of unsteady flows is the triple decomposition procedure [17]. For a generic variable q,

$$q(t) = \bar{q} + < q(t) > + q'(t) \tag{1}$$

where $\bar{q}$ is the time-averaged value, $< q(t) >$ is the purely periodic component associated with a coherent periodic structure, and $q'(t)$ is the random fluctuation associated mainly with turbulence. In rotating machinery, a shaft encoder is commonly used (see, for example, the early works of [18,19]) to provide a reference signal to extract the fluctuations induced by the rotor by means of a phase-averaging procedure. The phase-averaged value $\tilde{q}$ is equal to

$$\tilde{q} = \bar{q} + < q(t) > \tag{2}$$

This decomposition is used to characterize a single source of periodic unsteadiness (i.e., it allows isolating the effects of each rotor in cases of more than one rotor shaft). Moreover, any source of unsteadiness not linked with the rotor rotational speed is smeared out by this operation, as might be the case for von Kármán vortices or blade vibrations.

In the case of a two-spool counter-rotating turbine, Eq. (1) can be extended to [9]

$$q(t) = \bar{q} + < q(t) >_{\mathrm{HP}} + < q(t) >_{\mathrm{LP}} + \\ + < q(t) >_{\mathrm{HP,LP}} + q'(t) \tag{3}$$

where the two distinct purely periodic components $< q(t) >_{\mathrm{HP}}$ and $< q(t) >_{\mathrm{LP}}$, namely, the coherent structures due to the HP and LP rotor, respectively, have their own period and frequency ($\mathrm{BPF_{HP}}$ and $\mathrm{BPF_{LP}}$, respectively). The term $< q(t) >_{\mathrm{HP,LP}}$ indicates the rotor–rotor interactions that generate energy content at the frequencies of the linear combination $i \cdot \mathrm{BPF_{LP}} + k \cdot \mathrm{BPF_{HP}}$ (with i and k integers and not zero), which are observed in two shaft facilities (e.g., [9,20]). To resolve the phase-averaged evolution of the flow, a particular averaging procedure is required: rotor synchronic averaging (RSA), as introduced in Lengani et al. [9], which takes into account the relative positions of the two rotors in an absolute reference system. In particular, it has been shown that the overall unsteadiness is resolved as

$$\tilde{q}_{\mathrm{RSA}} = \bar{q} + < q(t) >_{\mathrm{HP}} + < q(t) >_{\mathrm{LP}} + \\ + < q(t) >_{\mathrm{HP,LP}} \tag{4}$$

Lengani et al. [9] have proved that the RSA ($\tilde{q}_{\mathrm{RSA}}$) preserves the frequency content of all coherent structures due to the rotor–rotor interactions. Note that Eqs. (2) and (4) are written for ideal rotors with perfectly identical blades. In the case of a real rotor, where geometrical defects may occur because of the manufacturing, a term including the periodicity at the harmonics of the revolution speed should be included. This will be discussed in Sec. V.A.1.

B. Modal Theory

Classically, data in the time domain may be represented in the frequency domain. There, each source of deterministic fluctuations (e.g., $< q_{\mathrm{HP}} >$) is associated with an energy peak at a fixed frequency and its harmonics (e.g., $\mathrm{BPF_{HP}}$ and its harmonics). The logical extension of this commonly used transformation is the decomposition of the flowfield in temporal and spatial Fourier coefficients as recently shown by Courtiade et al. [15] and Lengani et al. [13]. This decomposition is based on the early acoustic theory [12], but it may be extended to all aerodynamic quantities. In fact, as experimentally observed by Lengani et al. [21], rotating patterns characterize all the aerodynamic quantities, components of the velocity, flow angles, and pressure fluctuations. In particular, for an ideal rotor with identical blades, the deterministic fluctuations of the generic variable q at a circumferential position θ are represented as the following Fourier series [22]:

$$q(\theta, t) = \sum_{n=-\infty}^{\infty} \sum_{m=-\infty}^{\infty} A(m, n) e^{inB\Omega t - im\theta} \tag{5}$$

where n is the harmonic index (one for the BPF, two for the 2BPF, etc.), Ω is the rotor angular velocity, $A(m, n)$ are the coefficients of the Fourier series for the harmonic n and circumferential mode m.

This decomposition describes the deterministic fluctuations of the variable q as a superposition of an infinite number of rotating patterns, where the number of lobes is given by successive values of m. Each m-lobed pattern rotates at the speed $(nB/m)\Omega$ required to generate the nth multiple of the BPF. According to this convention, positive modes correspond to a pattern rotating with the rotor direction, whereas, negative modes are related to a pattern rotating in the opposite direction. Furthermore, Tyler and Sofrin [12] showed

that the mode m of the spatial Fourier decomposition is restricted to just some particular values:

$$m = nB + kV, \quad \text{with} \quad k = \ldots, -1, 0, 1, \ldots \tag{6}$$

where a simple stator–rotor interaction is considered, B is the number of rotor blades, and V is the number of stator blades.

It is possible to consider the interactions of the rotor with a complete vane assembly by simply superimposing the effects of a single event. For example, in a turbine, a mode m^* generated by a stator–rotor interaction will be scattered in the modes $m = m^* + kV_2$, with $k = \ldots, -1, 0, 1, \ldots$ by the following stator rows. Hence, for a stator–rotor–stator assembly, the following modes are predicted:

$$m = nB + k_1V_1 + k_2V_2, \quad \text{with} \quad k_1, k_2 \text{ integer} \tag{7}$$

where V_1 and V_2 are the number of vanes of the first and second stator row, respectively. A further extension of the present theory is provided by Holste and Neise [23]. They described the possible modes that may propagate in cases of rotor–rotor interaction with different rotational speeds, counter- or corotating.

C. Analogy with Conventional Decomposition

The generic Eq. (1) decomposes the flow at a fixed measurement position in a time-mean term $\bar{q}$, a term related to deterministic stresses $< q(t) >$, and a term related to stochastic stresses $q'(t)$. The application of this decomposition to a turbomachinery component (e.g., Adamczyk [24]), where there is the need for absolute and relative reference frames and the flow is not uniform circumferentially, leads to a multitude of terms to be taken into account in a numerical simulation. The degree of approximation of the problem depends on the number of such terms considered. Recently, it has been shown that numerical solutions based on Fourier methods (e.g., He [25]) are optimal approximations of the problem leading eventually to fast predictions in a multidisciplinary design.

The decomposition approach of Eq. (5) presents a strong analogy with Eq. (1) and is based on Fourier decomposition: it highlights temporal and spatial (circumferential) periodicity in the frequency/circumferential mode domain. Performing an analogy with numerical methods, the set of coefficients $A(m, n)$ from Eq. (5) is the sum of various contributions:

1) The frequency zero (time-mean value) and circumferential mode zero (circumferential-averaged value) correspond to the axisymmetric term of the model of Adamczyk [24].

2) The frequency zero (time-mean value) and circumferential mode different from zero correspond to the average stator-to-stator flowfield that arises from circumferential gradients induced by the stator rows.

3) The unsteadiness due to the rotor and its interactions with the stator rows corresponds to the sum of the modes $A(m, n)$ at all the multiples of the blade passing frequency.

This last contribution corresponds to the deterministic unsteadiness and it is composed of the multiples of the blade passing frequency. It may be further decomposed, considering Eq. (7), into the following two terms:

3') For k_1, k_2 equal to zero, the modes $m = nB$ at the rotational speed $(nB/m)\Omega$ correspond to the average rotor blade passage flow. For example, at the BPF, a mode corresponding to the blade number is observed; at two times the BPF, a mode corresponding to two times the blade number is observed, and so on. All these modes rotate at the rotational speed of the rotor [Eq. (5)], therefore, they are the trace of the rotor signal.

3") For k_1, k_2 not equal to zero, all the lobed structures arising from the stator/rotor interactions are identified.

Similarly, in a simulation based on Fourier methods, the rotor blade flow is solved in the relative frame of reference (term 3') and phase lag periodic conditions are applied to account for stator/rotor interactions (term 3").

In the case of rotor–rotor interaction, the harmonic index n of the set of coefficients $A(m, n)$ has to be changed. In this case, $A(m, n)$ has to be computed at the interaction frequencies $i \cdot \mathrm{BPF_{LP}} + k \cdot \mathrm{BPF_{HP}}$ (with i and k integers and not zero). This term could be used to resolve the passage-to-passage interactions of the relative reference frame.

III. Experimental Apparatus and Methodology

A. Facility

The transonic test turbine facility installed at Graz University of Technology is a continuously operating two-stage, cold-flow, open-circuit plant, which consists of a transonic HP stage and a counter-rotating LP stage. This unique configuration allows the testing of rig inserts under aerodynamic conditions relevant for modern aero-engine. Part 1 [1] provides the details on the operating condition at which the facility is operated during this measurement campaign. Further details on the facility and on the turbine configuration may be found in Hubinka et al. [26,27].

For completeness, a sketch of the tested turbine stages, together with the measuring planes adopted in the present paper, is reported in Fig. 1. The figure indicates the position of the different measurement techniques: the fast-response pressure probes and a laser vibrometer in cross-sectional planes (marked as C and D) and Kulite sensors mounted on the strut surface. The number of blades and vanes, which will be largely used to describe the modal decomposition results, is also reported in the picture.

B. Measurement Techniques

As described in the companion paper [1], unsteady flow measurements were performed by means of fast-response aerodynamic pressure probes. The present paper describes the results obtained with a cylindrical one-sensor probe (see Persico et al. [28] for more details). The probe was operated as a virtual three-sensor probe: the periodic fluctuations of velocity, pressures, and flow angles are determined from averaged values of the three rotations of the probe and its calibration matrix. The central position of the probe was aligned with the mean flow direction determined in a preliminary measurement campaign with a five-hole probe. This procedure provides a direct measurement of the total pressure and it can be used to perform the spectral analysis of the instantaneous total pressure. The present paper describes the results obtained by the fast-response probe in annular sectors in planes C and D (marked in Fig. 1). Details of plane position, measurement locations, and probe uncertainty are provided in part 1 [1].

As previously mentioned, the measurement campaign included the simultaneous acquisition of data from a laser vibrometer located at a fixed circumferential position in plane C and the one-sensor probe

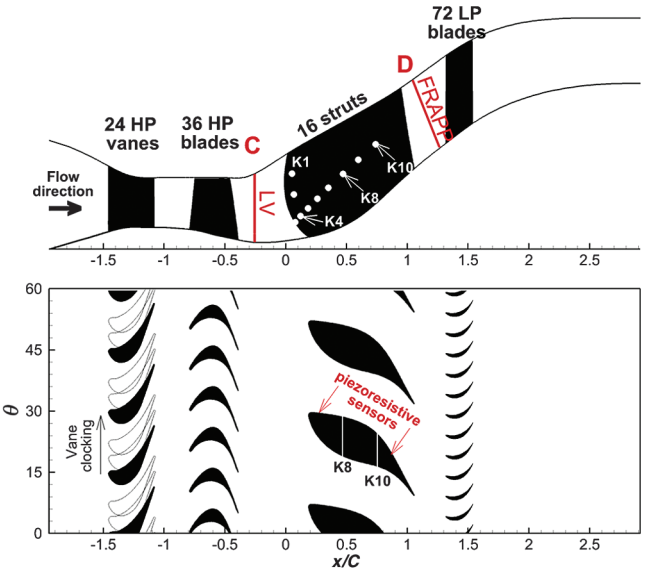

Fig. 1 Two-stage turbine test rig with measurement location.

located in plane D (which is fully traversed). The laser vibrometer is manufactured by Polytec (Waldbronn, Germany) and consists of a sensing head OFV-353 and a velocity decoder OFV-3001; it was set to a calibration factor 5 $\mathrm{mm}/(\mathrm{s}\cdot\mathrm{V})$, with maximum bandwidth and no optical filters applied. The vibrometer was set up to measure in the radial direction through a glass window. The laser beam was reflected on the surface of the machine hub, where a retroreflective foil was applied for a better signal strength.

Laser vibrometers, as employed in this investigation, consist of a Mach–Zehnder interferometer and were originally developed to detect surface vibrations from machinery, but they can also detect density fluctuations of a gaseous medium [29,30]. With the help of an acoustic-optical modulator, these interferometers record vibration velocity rather than surface amplitude, which provides a spectral signal increased by a factor of $2f$, with f being the frequency of the oscillation. In all types of interferometers, the optical path change between measurement and reference beam is recorded. The optical path passed by the laser beam can be calculated by multiplying the geometrical path with the refractive index of the gas. Therefore, in interferometry, not only changes of the geometrical path matter, but also changes of the refractive index. In gases of known composition, the refractive index is linked to changes of density via the Gladstone-Dale constant. When the laser beam from such a laser vibrometer is reflected by a rigidly fixed mirror or retroreflective foil, the output voltage represents the integral value of all density fluctuations along the beam path. The voltage output of the velocity decoder is given by

$$U(t) = \frac{2G}{k}\int_x \frac{\mathrm{d}\rho}{\mathrm{d}t}\,\mathrm{d}x \tag{8}$$

with the voltage U, the time t, the Gladstone–Dale constant G, the coordinate in the laser light beam direction x, and the density ρ. The Gladstone–Dale constant relates the gas density and refractive index. Only the signal changing in time contributes to the voltage signal provided by the velocity decoder, meaning that the vibrometer can only detect fluctuations rather than total density levels. Because the vibrometer integrates all fluctuations along the line of sight of the laser beam, no local values can be recorded with this setup. A second LV would be necessary to measure local density fluctuations within the point of intersection, as in Hampel and Woisetschläger [30].

C. Data Reduction Method

Data are acquired at 200 kHz and for 2 s, corresponding to more than 100 revolutions of the LP turbine and more than 350 of the HP turbine. An analog low-pass filter (80 kHz) has been applied to the FRAPP and LV signals to prevent aliasing. The FRAPP and LV signals, and the two shaft encoders, were acquired simultaneously to provide the frequencies of rotation of the two shafts. The measurement allows the decomposition of the flow with respect to the phase of one of the two rotors, hence, the effects of the two rotors on the flow may be observed separately. Furthermore, it also allows the reconstruction of a phase that takes into account the relative rotor–rotor positions (see Lengani et al. [9]).

Conventional fast Fourier transform (FFT) was applied to the FRAPP signal as well as to the LV signal. The cross-correlation coefficient $K(f)$ used later on is defined as follows:

$$K(f) = \frac{|\overline{C(f)}|}{\sqrt{|F_{\mathrm{FRAPP}}(f)|^2\cdot|F_{\mathrm{LV}}(f)|^2}} \tag{9}$$

where $C(f)$ is the complex cross correlation of both signals in the frequency domain, and $F_{\mathrm{FRAPP}}(f)$ and $F_{\mathrm{LV}}(f)$ are the individual signals in the frequency domain of the FRAPP and the laser vibrometer, respectively. The cross-correlation coefficient is a nondimensional measure of how well two signals correlate (basics of coherence theory can be found in Hecht [31]). The cross-correlation analysis was performed using a sample length of 2048 samples and providing frequency spectra for each FRAPP position traversed. The values are averaged from around 190 data blocks to provide a high accuracy with a reasonable frequency resolution.

Fourier transforms of phase-averaged or raw FRAPP data are shown through the paper. The criteria of these different analyses are provided in the dedicated sections. Because of the large number of samples and revolutions on which the phase averages are performed, the accuracy of the computed spectral amplitude stays within $\pm 2\%$ of the measured valued.

D. Modal Decomposition of the Flow Field

The modal theory has been developed for the pressure field (see Tyler and Sofrin [12]). However, as experimentally observed by Lengani et al. [21], rotating patterns characterize all the aerodynamic quantities, components of the velocity, flow angles, and pressure fluctuations. Hence, the decomposition of Eq. (5) may be applied to the aerodynamic field. For example, continuing the analogy with Fourier methods, Hall et al. [32], represented the flow variables as a Fourier series in time with spatially varying coefficients to satisfy the temporal periodicity of the flow in a time-harmonic balance computational method.

On the basis of the modal theory, a double Fourier decomposition method has been developed in Lengani et al. [13] and extended for restricted circumferential measurement domains in Lengani et al. [14]. For every radial and circumferential position of the measurement mesh, a discrete Fourier transform is applied to the phase-averaged generic flow quantity q (normalization factors are omitted in the formulation):

$$q(f)_{\theta,r} = \sum_{n_t} q(t)_{\theta,r} e^{-in_t f} \tag{10}$$

where the limits of the integration are defined by the number of points n_t within the revolution period, obtained from the phase-averaging procedure. This is the classic discrete Fourier transform in time, which reveals the frequencies that characterize the flowfield.

A discrete Fourier transformation in the circumferential direction is applied to the complex number $q(\theta, r, f)$:

$$A(m)_{r,f} = \sum_{n_c} q(\theta)_{r,f} e^{-in_c m} \tag{11}$$

where the limits of the integration are defined now by the number of points n_c in the circumferential direction. The operation is performed at any frequency f and radius r, and the variable $q(\theta)_{r,f}$ is integrated over the circumferential position θ. The Fourier coefficients are a set of complex numbers that are functions of the frequency and of the radius at which the data are obtained. Data are computed for the full frequency range, however, for the sake of conciseness, the behavior of the coefficients $A(m)_{r,f}$ will be discussed at a selected frequency ($\mathrm{BPF_{HP}}$) and some selected radii.

In this formulation, the fluctuations of the generic variable $q(\theta)_{r,f}$ are written as complex numbers in the frequency domain. According to the Fourier transform theory, a transformation of complex numbers leads to values of $A(m)_{r,f}$ that are not symmetric with respect to the spatial frequency (namely, the modes m). Modes, as predicted by the modal theory, are then positive or negative, spinning in the same direction or in the opposite direction of the rotor, respectively, following the convention previously adopted.

Equation (11) may be applied to different circumferential boundaries, where the spatial extension of the boundary defines the minimum mode computable. In fact, the minimum mode computable, except for mode 0, is directly proportional to the circumferential arc adopted in the decomposition (Nyquist–Shannon theorem). For example, measurements across a sector of 90 deg will lead to a minimum computable mode equal to four. Similarly, the number of circumferential points defines the maximum mode computable. Therefore, it is easy to demonstrate that all the modes of interest are computed when Eq. (11) is applied to the blade/vane count periodicity condition of a test rig.

Lengani et al. [14] showed that the limits of the Nyquist–Shannon theorem may be circumvented under the proper conditions: the modes of interest can be computed even when Eq. (11) is applied to a circumferential domain lower than the blade/vane count periodicity

using the nonlinear sampling theorem of Candés et al. [33] for sparse signals. However, in the present investigation, because of the mechanical complexity of the two-spool turbine and because of the complexity of the interactions, the method described in Lengani et al. [14] would resolve just some of the modes to be observed in plane D. Therefore, the modal decomposition results shown in the result section for plane D are obtained from a numerical investigation.

IV. Numerical Techniques

The numerical investigation was performed with a commercial CFD code (CFX 12.1). The computational grid consists of 14 million elements divided in five domains (two rotating for the rotors and three stationary for the vanes and the outflow), all of them with 90 deg periodicity. The mesh adopted for the unsteady computation is similar to the mesh provided in Spataro et al. [34] for a steady computation, but extended to the 90 deg periodicity and to the HP stage. A grid refinement study was performed for the steady CFD, as described by Spataro et al. [34].

The unsteady simulation required about 28 GB of memory. The y^+ was kept below one next to the blade surface and below two next to the endwall. The code solves the Navier–Stokes equation system with first-order accuracy in areas where the gradients change sharply to prevent overshoots and undershoots and maintain robustness, and second-order accuracy in flow regions with low variable gradients to enhance accuracy [35]. The turbulence model used was the shear stress transport k-ω model by Menter [36]. The unsteady flow was computed by second-order backward equations: the time step was chosen as $1/100$ of the high-pressure rotor blade passing period. The conditions at the inlet and outlet boundaries were taken from the experimental measurements performed by Santner et al. [37] and Hubinka et al. [27].

V. Results and Discussion

This section is divided into three main parts. The first part concerns the analysis of the unsteady deterministic fluctuations in the frequency domain. It looks at amplitude and phase of the Fourier transform from time to frequency domain. The amplitude spectra shown in the following figures are normalized by the amplitude at the blade passing frequency of the HP rotor $\mathrm{BPF_{HP}}$ in plane C (downstream of the HP rotor) at midspan. This is done to provide a direct measurement of the decay of the HP rotor deterministic unsteadiness. The second part consists of the modal analysis results. The results of this decomposition are the complex numbers $A(m)_{r,f}$ of Eq. (11). Their amplitude is sufficient to describe and identify the characteristic spatial wave length. Their phase is not shown or commented on. Note that the amplitude and phase of $A(m)_{r,f}$ provide the full spatial/temporal evolution of the flow (for a discrete radius). For this reason, a tough validation of CFD results in plane C is provided by comparing the amplitude of $A(m)$ for CFD and FRAPP at different radii, to extend the validation approach provided in the companion paper [1]. The last part provides some considerations on the transport and decay of the unsteadiness, summarizing the results discussed in the previous two parts.

A. Frequency Analysis

1. Plane C: HP Rotor Outlet

Figure 2 shows nondimensional amplitude spectra obtained from averaging 20 measurement positions at midspan downstream of the HP rotor (one radial position). Two different experimental spectra are shown, and the amplitude of CFD results at select frequencies is also reported (red dots). The spectrum in black (marked FRAPP, raw signal on the plot) was determined from the raw signal of the probe aligned with the mean flow. This corresponds to the spectrum of the total pressure because the FRAPP directly measures the total pressure within a certain flow angle range (± 10 deg in the present case). Downstream of the HP rotor, the phase-resolved variations of the flow angle were measured in a preliminary test with the FRAPP. At midspan, they are within the probe insensitivity range, which means that the instantaneous total pressure signal is acquired aligning the probe with the mean flow angle. The blue spectrum (marked FRAPP, PLA signal, representing the phase-locked-average signal) is obtained from the phase-averaged signal comprising exactly 32 revolutions of the HP rotors. In this case, the frequency resolution of the spectrum is a submultiple of the rotational speed (i.e., $1/32$ of it in the present case). The rotational speed may be identified on the plot as the first engine order (EO $= 1$).

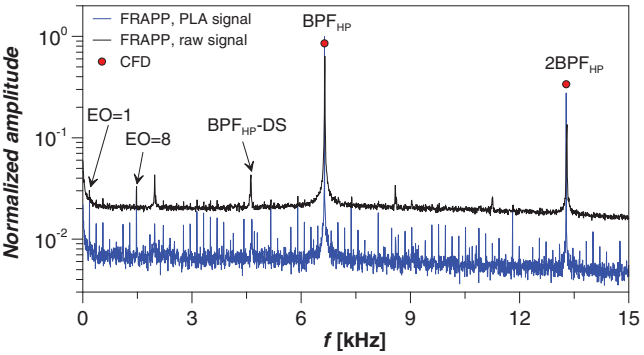

Fig. 2 Normalized amplitude spectra, plane C at midspan.

The largest amplitude is measured for both experimental spectra at the blade passing frequency ($\mathrm{BPF_{HP}}$) and its harmonic ($\mathrm{2BPF_{HP}}$). Amplitude peaks at lower frequencies are also identified, corresponding to the first and eighth EO (EO $= 1, 8$, on the plot). These two peaks may be observed for both spectra, but they are more evident for the spectrum of the phase-locked-average signal. They represent geometrical asymmetries of the rotor disk and blade. Their amplitude is about 20 times lower than the amplitude of the signal at the blade passing frequency. It should be noted that, because the HP blades are transonic, the generation of shock waves increases the sensitivity to small geometrical asymmetries (see, for example, McAlpine and Fisher [38]). Hence, the HP rotor has been manufactured with a very high geometrical precision.

Amplitude peaks at other harmonics of the EO, which are of lower amplitude, can be observed as sharp peaks just in the PLA spectrum. This is because the stochastic fluctuations exceed the deterministic contribution at these frequencies for the raw data. The difference between the spectrum of the raw signal and the one from PLA is proportional to the stochastic component of the signal.

The raw signal spectrum identifies further amplitude peaks at around 2.0, 4.6, 8.6, and 11.2 kHz. These peaks are not related to the rotor rotational speed, in fact, the amplitude at these frequencies of the PLA signal is much lower. Therefore, these frequencies represent deterministic fluctuations not related to the HP rotor rotation. To the knowledge of the authors, similar spectra, with peaks unrelated to the blade passing frequencies, were measured by Davis et al. [5], Kielb et al. [39], Southworth et al. [40], and Green et al. [41]. However, in these papers, there are no further comments or analyses about the source of these deterministic fluctuations.

2. Plane D: TMTF Outlet

Downstream of the TMTF, the amplitude spectrum of the raw signal of the FRAPP aligned with the mean flow angle shows peaks at the HP rotor blade passing frequency and its harmonics. It also shows peaks of smaller amplitude, the source of which cannot be identified from the analysis of the raw signal only. For this reason, the spectrum of Fig. 3 and the cross-correlation coefficient of Fig. 4 are derived by different means to isolate the sources of unsteadiness. The amplitude spectrum shown in Fig. 3 is obtained from the FRAPP signal after phase averaging with the RSA procedure [see Eq. (4) and Lengani et al. [9] for more details]. The RSA signal length corresponds to three revolutions of the LP rotor, which is about nine revolutions of the HP rotor. Hence, the frequency resolution is less than one-third of the frequency resolution provided in Fig. 2. The cross-correlation coefficient of Fig. 4 is defined in Sec. III.C. The two plots show averaged values of the 45 circumferential measurement positions at midspan.

The RSA procedure has been developed to provide a signal that takes into account the deterministic unsteadiness related to the two

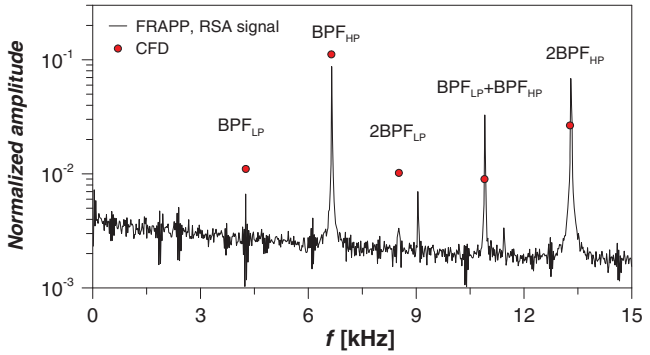

Fig. 3 Normalized amplitude spectra, plane D at midspan.

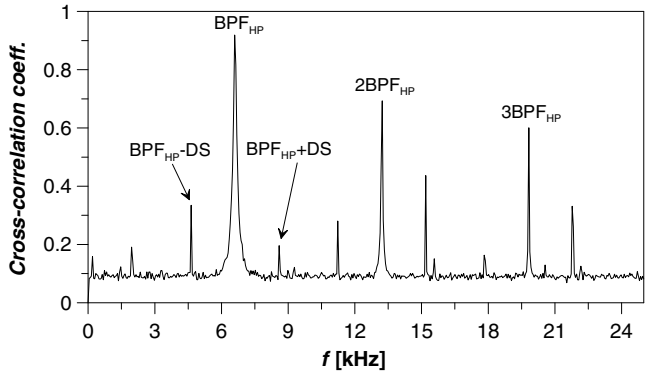

Fig. 4 Cross-correlation coefficient (coeff.) between FRAPP (plane D at midspan) and LV (plane C).

rotors [see Eq. (4)]. Therefore, the Fourier transform of the signal shows amplitude peaks at the linear combinations of the blade passing frequencies of the two rotors $i \cdot \mathrm{BPF_{LP}} + k \cdot \mathrm{BPF_{HP}}$ (with i and k integers). The highest amplitude occurs at the blade passing frequency of the HP rotor ($\mathrm{BPF_{HP}}$). Further, a peak of lower amplitude is visible for the $\mathrm{BPF_{LP}}$; this reveals that the unsteadiness of the LP rotor propagates upstream. Because of this, there are also relatively high-amplitude peaks of the periodic contributions due to the rotor–rotor interaction: the amplitude of $\mathrm{BPF_{HP}} + \mathrm{BPF_{LP}}$ is about half the amplitude of the $\mathrm{BPF_{HP}}$, and the contribution at $2\mathrm{BPF_{HP}} - \mathrm{BPF_{LP}}$ has an amplitude comparable to the contribution at the $\mathrm{BPF_{LP}}$. Figure 3 also provides the amplitude of CFD results at the mentioned frequencies. The agreement between experimental and numerical results is fairly good, considering the complexity of the flowfield. The CFD starts to deviate from experimental results for higher frequencies (above $\mathrm{BPF_{HP}} + \mathrm{BPF_{LP}}$).

The cross correlation in Fig. 4 shows different information. It describes which deterministic contribution measured downstream of the HP rotor (by the LV) propagates through the duct. It takes into account deterministic contributions not necessarily related to the two rotor unsteadiness. The largest value of the cross-correlation coefficient is measured at the blade passing frequency of the HP rotor. At the sides of this frequency, two peaks are observed, and they are shifted from the $\mathrm{BPF_{HP}}$ by about ± 2 kHz. This frequency shift, considering the rotor tip speed and the celerity of sound in plane C, corresponds to the change in frequency due to the Doppler shift (DS). For this reason, the peaks are marked in the figure as $\mathrm{BPF_{HP}} - \mathrm{DS}$ and $\mathrm{BPF_{HP}} + \mathrm{DS}$. The presence of traveling reflected waves has been documented in CFD investigations (e.g., Göttlich [4] and Davis et al. [5]), performed in the HP rotor followed by a diffusing duct. However, in these previous investigations, it is not pointed out at which frequency (or combination of frequencies as observed here) they should occur or if they can travel downstream. The result of Fig. 4 clearly demonstrates that they can travel downstream and that peak frequencies due to this phenomenon occur at a linear combination of the Doppler shift and the blade passing frequency of the HP rotor. Note that the same physical phenomenon was measured in plane C with the FRAPP (see the peak marked with $\mathrm{BPF_{HP}} - \mathrm{DS}$ in Fig. 2). However, the presence (intrusive character) of the probe in the measurement plane was slightly altering its frequency (compare Figs. 2 and 4). The frequency of the Doppler shift is better resolved with the laser vibrometer because it is a nonintrusive measurement.

The phase of the cross correlation between the FRAPP and LV signals, which is depicted at the $\mathrm{BPF_{HP}}$ in Fig. 5, provides a further information. Figure 5a shows the phase of the cross-correlated signal for the full measurement plane to highlight this aspect. The wave front is constant at the different radii, small distortions occur in the position of the strut wake (marked on the plot). The phase changes its sign from $\theta/\Delta\theta_{\mathrm{Strut}} = 0.1$ to 0.9, assuming values that range from π to $-\pi$. The phase shift is observed between the pressure side boundary layer of the strut (marked as PS on the plot at $\theta/\Delta\theta_{\mathrm{Strut}} = 0.1$) and the pressure side of the adjacent strut vane (marked PS at $\theta/\Delta\theta_{\mathrm{Strut}} = 0.9$). Clearly, this phase shift has a different periodicity than that of the strut (or the HP vane and rotor).

The phase shift is representative of a plane wave propagation front, which is schematically represented in the sketch in Fig. 5b. The wave front propagation is orientated perpendicular to the rotor wakes (compare it with Figs. 7a and 9a of part 1 [1]). However, the periodicity of the wave front differs from the periodicity of the vane or rotor. These results imply that the pressure wave propagation at the outlet of the strut depends on HP stage/strut interaction, as it will be discussed in the modal analysis section.

3. *Vane–Vane Clocking*

As observed in part 1 [1], the pressure fluctuations on the strut surface depend strongly on their relative position with respect to the HP vane. Therefore, the unsteady pressure field at the outlet of the strut should depend on vane–rotor–vane interaction. Figure 6 represents the normalized amplitude of the pressure fluctuations of the Kulite sensors mounted on the strut surface. This information is extracted from the FFT peak at the blade passing frequency of the HP rotor and its harmonic. Information at the $2\mathrm{BPF_{HP}}$ are extracted just for the sensors located in the strut inlet section, because the amplitude at this frequency becomes less relevant on the suction side (SS) surface.

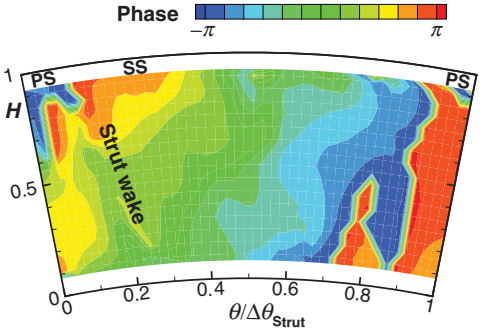

a) Phase of cross-correlated signal

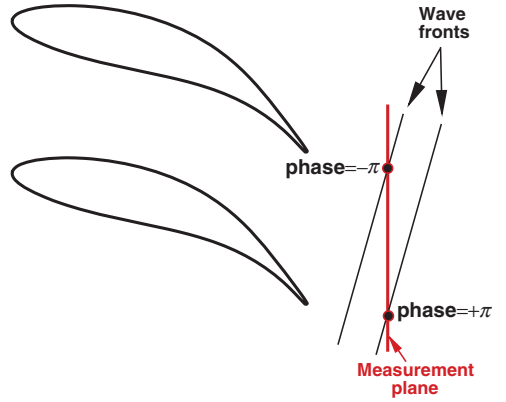

b) Schematic representation of wave front propagation

Fig. 5 FRAPP and LV results in plane D: measured phase and schematic exemplification.

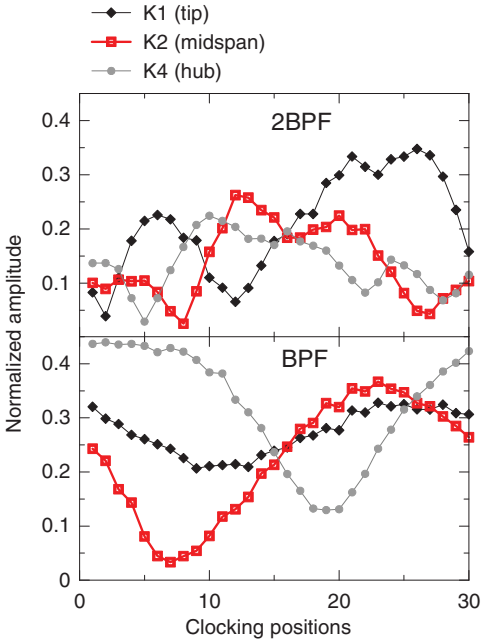

a) TMTF inlet: BPF_{HP} (bottom), $2BPF_{HP}$ (top)

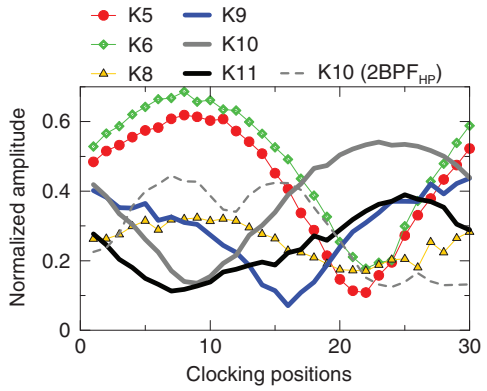

b) TMTF suction side: BPF_{HP}

Fig. 6 Normalized amplitude of Kulite sensors mounted on the TMTF for different clocking positions.

Figure 6a shows the pressure fluctuations amplitude at the strut leading edge for three different positions along the span and for the two frequencies. This picture summarizes the effects described in part 1 [1] for the 30 clocking positions analyzed. The impact of vane clocking on the fundamental frequency is quite large at the hub and midspan: variations of the clocking position lead to large relative variations in amplitude (e.g., at midspan the maximum amplitude is up to six times the minimum amplitude). At the tip, the pressure fluctuations depend less on the clocking position. The opposite situation is shown for the harmonic ($2BPF_{HP}$ on top of the picture); the largest variations and amplitude at this higher frequency are measured at the tip. As discussed in part 1 [1], the tip leakage vortex leads to high-amplitude fluctuations covering a wide frequency range. Otherwise, the fluctuations at the hub, caused by the HP vane secondary flows and the shock system, are more sensitive to variation of the relative vane–vane position at the BPF_{HP}. It appears that it seems very hard to find a position of optimal clocking, namely, a position to minimize the unsteady forcing over the entire span in this inlet section.

A similar trend is shown for the Kulites mounted on the strut suction side along a streamline. The sensors close to the leading edge (K5 and K6 of Fig. 6b) have the maximum amplitude for clocking position 9 (as described in part 1 [1]). On the other hand, the downstream sensors (K10, K11) measure the highest pressure fluctuations for clocking position 24. The amplitude at the 2 BPF_{HP} is shown for sensor K10 (dashed gray): this is the only position along the strut suction side for which the fundamental frequency and its harmonic have comparable amplitude. As observed in Haldeman et al. [6] and Lavagnoli et al. [7], the fundamental frequency typically shows the highest amplitudes, however, this kind of analysis cannot neglect a priori the higher order harmonics.

The general trend, as also documented in the aforementioned works, does not show a clocking position for minimizing the overall forcing on the vane. Furthermore, two adjacent struts face two different clocking positions [1]. For example, considering the vane count of the present configuration, when the strut under investigation faces clocking position 9, the adjacent strut faces position 24. This implies limits in reducing the overall forcing at a specific section (e.g., the outlet) of the struts.

B. Modal Decomposition: Analysis

The previous section discussed which deterministic unsteadiness propagates (up- and downstream) through the duct. Different sources of deterministic stresses have been identified: the largest pressure fluctuations are due to the HP rotor, other sources such as reflected shock waves and rotor–rotor interactions at a recognized periodicity (BPF_{LP}, $BPF_{HP} + BPF_{LP}$, $2BPF_{HP} - BPF_{LP}$) also propagate downstream. As observed in part 1 [1], and as also introduced here discussing the effect of vane–vane clocking, the unsteadiness at the outlet of the TMTF is the result of a complex vane–rotor–vane interaction. This is why, for example, the phase of the FRAPP+LV cross correlation incompletely solves the problem of unsteadiness propagation within the duct. In Sec. V.A.2, a wave front is identified, however, it is not circumferentially periodic within the strut passage. In the two following subsections, the unsteadiness at the fundamental BPF_{HP} is decomposed according to Eq. (5) in spinning lobed patterns of well-defined spatial frequencies (the modes m). The number of such "spinning modes" is limited and they are associated with different sources of unsteadiness. They allow the identification of the unsteadiness due to the rotor alone and that due to the vane–rotor (or rotor–vane) interaction. To isolate these different sources, the analysis starts with plane C (just downstream of the rotor), where the unsteadiness is generated by the HP stage only because the potential effects of the downstream strut are negligible. Afterward, plane D is discussed.

1. *Plane C: HP Rotor Outlet*

The results of the modal decomposition performed in plane C from the CFD and FRAPP data are shown in Fig. 7 considering the

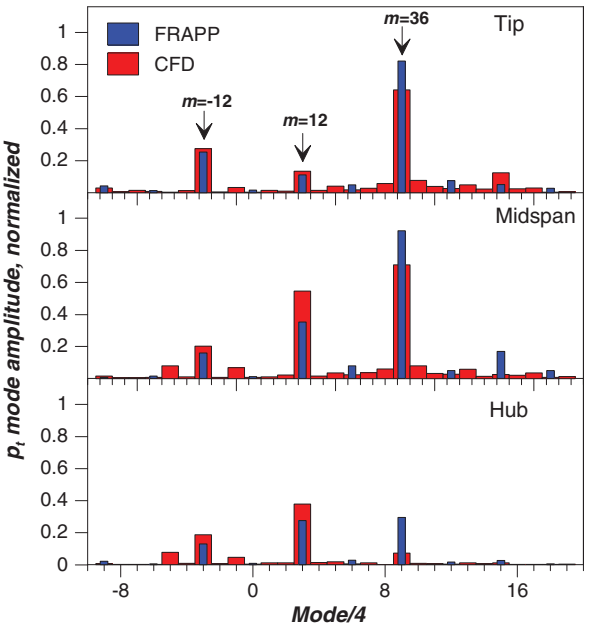

Fig. 7 Circumferential mode amplitude of total pressure obtained from CFD and FRAPP data at BPF_{HP}, plane C.

fundamental frequency BPF_{HP}. As previously explained, the CFD simulation was performed for 90 deg, which corresponds to the rig periodicity; the resolution of the decomposition is then set to correctly resolve the modes of interest [see Eqs. (6) and (7)], multiples of 4. Similarly, the experimental data, acquired on a reduced circumferential domain, were treated to correctly solve just the modes of interest generated by HP vane/HP rotor interaction.

The figure shows the amplitude of the modal decomposition of the total pressure at three different positions along the span. The amplitude is normalized, as in all previous plots, with the amplitude at the BPF_{HP} of the average FFT in plane C at midspan. The circumferential mode amplitude is plotted on the abscissa dividing it by four, according to the resolution of the decomposition. However, the actual mode number will be referred to in the discussion (e.g., mode 36 corresponds to value 9 read on the graph axis). To make the graph more readable, the modes of interest are labeled in the picture.

The spatial mode generated by the HP stator/HP rotor interaction are predicted using Eq. (6). This interaction consists of the linear combination of modes $m = B + kV = 36 + k \cdot 24 = \ldots -36; -12; 12; 36 \ldots$. The mode 36, as previously observed, corresponds to the lobed structures at the same spatial periodicity of the rotor blade that spins at the rotor rotational speed. Hence, the mode 36 is the trace of the "rotor-alone" unsteadiness. On the other hand, the modes $-12, 12$ are related to the lobed structures of a different circumferential periodicity and, therefore, they are generated by the vane–rotor interaction only.

The first result observed is that the modes at the BPF_{HP} are mainly limited to three modes: $-12, 12, 36$ (consider both CFD and FRAPP results). Higher order modes, predicted by Eq. (6), such as -36 or 60, have a much lower amplitude. At the tip and at midspan, the largest amplitude is observed for the rotor-alone structures (mode 36). As discussed in part 1 [1] and observed in Fig. 6a, the upper portion of this measurement plane is dominated by the secondary flows (tip leakage vortex and upper passage vortex) of the HP rotor. Hence, the trace of the stator–rotor interaction plays a minor role in the unsteadiness generation in these measurement positions. The trend at the hub is different; the experimental data show that modes 12 and 36 have almost the same amplitude, and the CFD data underestimate the amplitude of mode 36. The different distribution of the mode amplitude in the hub position is due to the flow turning imposed by the S-shaped duct, which leads the rotor unsteadiness toward the outer casing. Indeed, the overall unsteadiness at the hub is much lower than in the upper portion of the channel. It is important to highlight that the present analysis leads to the validation of CFD data simply comparing the amplitude of three modes in a very concise manner, being more exhaustive than the validation provided in Fig. 3 of the companion paper [1].

The modal decomposition provides a fast validation of the CFD result. The amplitude and phase of $A(m)_{r,f}$ provide the full spatial/temporal evolution of the flow (for a discrete radius). Hence, the comparison of mode amplitude between experimental and numerical results corresponds to the comparison of two time-space plots reduced to a comparison of three modes (in this case) for the fundamental frequency of the HP rotor. Considering this, the agreement is fairly good: the trend and amplitudes of the modes are very well predicted by CFD except for the hub position, where the trend between the amplitude of modes 12 and 36 is not in agreement.

2. *Plane D: TMTF Outlet*

Downstream of the TMTF, the unsteadiness of the HP rotor has not decayed, as observed from Fig. 3. In this setup, HP stage and LP vane, the unsteady flow is represented by a complex pattern due to stator–rotor–stator interactions. Equations (6) and (7) predict, at the BPF_{HP}, the following modes:

1) HP stator–HP rotor interaction consists of the modes $36 + k \cdot 24\times = \ldots -36; -12; 12; 36 \ldots$.

2) HP rotor–TMTF interaction consists of the modes $36 + k \cdot 16\times = \ldots -28; -12; 4; 20; \ldots$.

3) HP stator–HP rotor–TMTF interaction consists of the modes $36 + k_1 \cdot 24 + k_2 \cdot 16 = \ldots -28; \quad -20; \quad -12; \quad -4; 4; 12; 20; 28 \ldots$

All of these different interactions may be observed in Fig. 8. In this plane, the mode amplitude is obtained just from CFD. As previously explained, the mechanical complexity of the rig and of the unsteady interaction did not allow the modal decomposition of FRAPP data. Note that the scales on the axes of Figs. 7 and 8 are different. This is necessary because the amplitude of the fluctuations is considerably reduced in the outlet plane, as well as the mode structure is changed.

The most striking feature of Fig. 8 is that mode 36, the rotor-alone trace, is completely decayed, whereas in plane C, this was the mode with the largest amplitude. The predominant modes, marked in the top plot, are $m = -20, -12, 12$. Therefore, the lobed structure of the unsteadiness propagating through the duct depends strictly on the vane–rotor–vane interaction. Among the largest amplitude modes, just mode -12 is predicted by HP rotor–TMTF interaction. However, the mode $m = -12$ was already observed in the upstream plane and generated by HP stator–HP rotor interaction.

The information provided by Figs. 7 and 8 must be coupled with the flow evolution within the duct [1]. Because of its S-shape, the flow structures of the upper portion of the channel in plane C are moving toward midspan in the outlet plane. Similarly, in the middle plot of Fig. 8, the amplitude of mode -12 is larger than that of mode 12. This trend corresponds to the trend of the same modes at the tip in Fig. 7.

The large amplitude of further modes (such as mode -20 at the tip) is caused by the vane–rotor–vane interaction. Mode -20 is not predicted by the HP stator–HP rotor interaction, neither by the HP rotor–TMTF interaction. Hence, the unsteadiness in this downstream plane is due mostly to the unsteady interaction of the HP rows, which is further scattered by the interaction with the strut. There seems to be a low influence of the HP rotor–TMTF interaction. As observed by other authors (e.g., Göttlich [4]), the pressure fluctuations of the HP stage, which are caused by the strong shock waves and secondary flows, do not decay within the duct. The present analysis highlights how the structures of the rotor alone and the interaction of the rotor with the strut play a minor role in the transport of unsteadiness.

C. Transport and Decay of Unsteadiness: Considerations

Figures 2, 3, and 6–8 report amplitude spectra (in the frequency or modal domain) normalized by the mean amplitude at the BPF_{HP} in plane C. Hence, each plot presents the decay of the unsteady fluctuation of pressure from the HP stage outlet to the inlet of the LP rotor. The amplitude at the fundamental frequency of the HP rotor is decaying of about one order of magnitude. The decay rate of the 2 BPF_{HP} is lower; the amplitude at this frequency is four times lower in

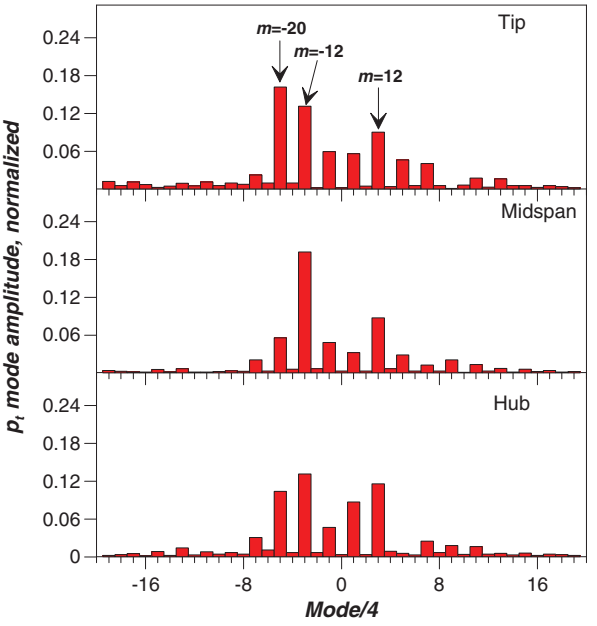

Fig. 8 Circumferential mode amplitude of total pressure obtained from CFD at BPF_{HP}, plane D.

the downstream plane. This decay rate seems quite large, however, it has to be considered that the unsteady pressure fluctuations induced by a transonic HP turbine stage are much larger than that induced by an LP stage. Hence, downstream of the LP rotor, as shown in Lengani et al. [9], the amplitude of the unsteadiness evoked by the HP stage is comparable with the one of the LP rotor.

The deterministic contributions at frequencies unrelated to the rotor rotational speed, which are due to a Doppler effect of reflected shock waves, are more highly damped. They still propagate and cannot be neglected because even the smallest amplitude deterministic fluctuations may excite vibrations.

The decay of unsteadiness is influenced by the local pressure gradient within the strut passage, as documented from Fig. 6 and in the companion paper [1]. The amplitude at the leading edge of the strut is overall lower than on the suction side surface at selected locations. Particularly, as shown in Fig. 9c of part 1, local maxima of the overall unsteady fluctuation, independent of clocking, are observed in sensors K6 and K10. Downstream, pressure fluctuations start to visibly decay from the strut throat (K10) to plane D because of the flow deceleration.

The modal spectra amplitudes (Figs. 7 and 8) provide further information related to the amplitude of the azimuthal spinning waves that propagate at the analyzed frequency (BPF_{HP}). In plane C (Fig. 7), the amplitude of mode 36 (rotor alone) is almost equivalent to the average spectra. The amplitude of the modes generated by the stator–rotor interaction (± 12) is below 50% of the average spectra. In plane D (Fig. 8), mode 36 completely decays, whereas the amplitude of modes ± 12 is halved. This last effect is not entirely due to the decay of unsteadiness but it may be related to mode scattering; indeed, further modes are generated through the duct by the HP stage–strut interaction [see Eq. (7)].

The decay of the average amplitude at the BPF_{HP} is mostly due to the vanishing of mode 36 (rotor-alone effects). Turbine characteristic parameters such as Mach number, frequency, and blade and vane number influence which mode decays or propagates and can be eventually chosen to damp out the larger deterministic stresses. The present analysis clearly explains why the introduction of splitter vanes within the strut passage [10,11] reduces the unsteady pressure fluctuations: the splitter vanes act as a cutoff to the propagating modes [reconsider Eq. (7)], altering the modal structure of the pressure waves that decay instead of propagate.

VI. Conclusions

This paper provided an analysis of the deterministic stress propagation through the turning midturbine frame of a counter-rotating turbine. Complementary measurement techniques have been performed at the outlet of the HP stage, on the strut suction side and at its outlet. The experimental data set provided has been applied for computational code validation. The time-resolved measurements and CFD results have been adopted to characterize the sources of unsteadiness from the exit of the HP stage to the inlet of the LP rotor. This second part paper is focused on the spectral analysis of the data reported in the companion paper [1]. This paper summarizes the theoretical background behind the modal decomposition of the flowfield and its capability to isolate the effects of the aerodynamic unsteady interactions between stator and rotor rows.

Different sources of deterministic frequencies and their amplitudes have been identified downstream of the HP stage. The largest amplitudes are classically related to the fundamental blade passing frequency of the HP rotor and its harmonics. However, frequencies at which relevant amplitudes occur have been identified in some harmonics of the HP rotational frequency and in a Doppler shift, due to reflected shock waves. Furthermore, a simultaneous measurement of a laser vibrometer and a fast-response pressure probe (up- and downstream of the strut, respectively) has been provided to verify the propagation of the deterministic stresses. It has been shown that these frequencies (harmonics of the blade passing frequency and Doppler effect), even though they lose amplitude, do not completely decay through the duct.

The effects of vane–vane clocking, which were described in more detail in the companion paper [1], are summed up in this second part paper. The spectral analysis confirmed that the largest amplitude fluctuations occur at the blade passing frequency of the HP rotor. Fluctuations at the strut leading edge are also characterized by energy content at higher harmonics of the fundamental frequency; the higher harmonics become less relevant on the strut surface. Overall, because of the three-dimensional effects of clocking and the complexity of the interactions, a position of optimal clocking (in the sense of minimum unsteady stresses on the strut) is difficult to find.

The final analysis consisted of the modal decomposition of the unsteady flowfield. With the present analysis method, the overall deterministic unsteadiness of the flow is simplified, even for complex multistage configurations, to a limited number of Fourier coefficients (modes) in time and space. The sources of the deterministic fluctuations can be observed and discussed with a limited number of modes. The unsteadiness related to the HP rotor-alone effects completely decay through the duct. On the other hand, the unsteadiness related to HP vane–rotor interaction does not decay, it is scattered by the interaction with the strut. The knowledge of the modal structure identifies which are the causes of the largest amplitude fluctuations (HP vane–rotor interaction in this case). Therefore, this analysis method may be used for the optimization process in a multidisciplinary design approach.

Acknowledgments

The research leading to these results has been funded by the European Union (EU) within the EU project DREAM (contract ACP7-GA-2008-211861) and the Austrian Science Fund project 24096-N24 "Interferometric Detection of Thermoacoustic Oscillations in Flames," as well as from the Austrian Ministry for Finance. The authors would like to thank Jakob Woisetschläger, H. Peter Pirker, Cornelia Santner, Josef Hubinka, and Berardo Paradiso for their important support during the experimental campaign.

References

[1] Lengani, D., Spataro, R., Paradiso, B., and Göttlich, E., "Unsteady Flow Features Evolution Through a Turning Midturbine Frame Part 1: Time-Resolved Flow," *Journal of Propulsion and Power* (to be published).

[2] Norris, G., Dominy, R. G., and Smith, A. D., "Strut Influences Within a Diffusing Annular S-Shaped Duct," *Proceedings of ASME Turbo Exposition 1998*, American Soc. of Mechanical Engineers Paper 1998-GT-425, Fairfield, NJ, 1998.

[3] Marn, A., Göttlich, E., Cadrecha, D., and Pirker, H. P., "Shorten the Intermediate Turbine Duct Length by Applying an Integrated Concept," *Journal of Turbomachinery*, Vol. 131, No. 4, July 2009, Paper 031006. doi:10.1115/1.3070578

[4] Göttlich, E., "Research on the Aerodynamics of Intermediate Turbine Diffusers," *Progress in Aerospace Sciences*, Vol. 47, No. 4, 2011, pp. 249–279. doi:10.1016/j.paerosci.2011.01.002

[5] Davis, R. L., Yao, J., Clark, J. P., Stetson, G., Alonso, J. J., Jameson, A., Haldeman, C. W., and Dunn, M. G., "Unsteady Interaction Between a Transonic Turbine Stage and Downstream Components," *International Journal of Rotating Machinery*, Vol. 10, No. 6, 2004, pp. 495–506. doi:10.1155/S1023621X04000491

[6] Haldeman, C. W., Krumanaker, M. L., and Dunn, M. G., "Influence of Clocking and Vane/Blade Spacing on the Unsteady Surface Pressure Loading for a Modern Stage and One-Half Transonic Turbine," *Journal of Turbomachinery*, Vol. 125, No. 4, Dec. 2003, pp. 743–753. doi:10.1115/1.1625398

[7] Lavagnoli, S., Yasa, T., Paniagua, G., Castillon, L., and Duni, S., "Aerodynamic Analysis of an Innovative Low Pressure Vane Placed in an S-Shape Duct," *Journal of Turbomachinery*, Vol. 134, No. 1, 2012, Paper 011013. doi:10.1115/1.4003241

[8] Praisner, T. J., Grover, E. A., Mocanu, R., Jurek, R. J., and Gacek, R. E., "Predictions of Unsteady Interactions Between Closely Coupled High Pressure- and Low Pressure-Turbines with Co- and Counter-Rotation," *Journal of Turbomachinery*, Vol. 135, No. 6, Nov. 2013, Paper 061008.

[9] Lengani, D., Santner, C., Spataro, R., and Göttlich, E., "Analysis Tools for the Unsteady Interactions in a Counter-Rotating Two-Spool Turbine

Rig," *Experimental Thermal and Fluid Science*, Vol. 42, Oct. 2012, pp. 248–257.
doi:10.1016/j.expthermflusci.2012.05.010

[10] Spataro, R., Göttlich, E., Lengani, D., Faustmann, C., and Heitmeir, F., "Development of a Turning Mid Turbine Frame with Embedded Design-Part I: Design and Steady Measurements," *Journal of Turbomachinery*, Vol. 136, No. 7, 2014, Paper 071008.

[11] Spataro, R., Göttlich, E., Lengani, D., Faustmann, C., and Heitmeir, F., "Development of a Turning Mid Turbine Frame with Embedded Design-Part II: Unsteady Measurements," *Journal of Turbomachinery*, Vol. 136, No. 7, 2014, Paper 071012.
doi:10.1115/1.4025950

[12] Tyler, J. M., and Sofrin, T. G., "Axial Flow Compressor Noise Studies," *SAE Transactions*, Vol. 70, 1962, pp. 309–332.

[13] Lengani, D., Selic, T., Spataro, R., Marn, A., and Göttlich, E., "Analysis of the Unsteady Flow Field in Turbines by Means of Modal Decomposition," *Proceedings of ASME Turbo Exposition 2012*, American Soc. of Mechanical Engineers Paper GT2012-68582, Fairfield, NJ, June 2012.

[14] Lengani, D., Kindermann, S., Selic, T., Marn, A., and Heitmeir, F., "Measurement and Decomposition of Periodic Flow Structures Downstream of a Test Turbine," *Experiments in Fluids*, Vol. 55, No. 1, 2014, Paper 1632.
doi:10.1007/s00348-013-1632-1

[15] Courtiade, N., Ottavy, X., and Gourdain, N., "Modal Decomposition for the Analysis of the Rotor-Stator Interactions in a High-Speed Multistage Compressor," *Journal of Thermal Science*, Vol. 21, No. 3, 2012, pp. 276–285.
doi:10.1007/s11630-012-0545-2

[16] Gougeon, P., and Ngo Boum, G., "Aerodynamic Interactions Between a High-Pressure Turbine and the First Low-Pressure Stator," *Journal of Turbomachinery*, Vol. 136, No. 7, July 2014, Paper 071010.
doi:10.1115/1.4025955

[17] Hussain, A., and Reynolds, W., "The Mechanics of an Organized Wave in Turbulent Shear Flow," *Journal of Fluid Mechanics*, Vol. 41, No. 2, 1970, pp. 241–258.
doi:10.1017/S0022112070000605

[18] Sharma, O. P., Butler, T. L., Joslyn, H. D., and Dring, R. P., "Three-Dimensional Unsteady Flow in an Axial Flow Turbine," *Journal of Propulsion and Power*, Vol. 1, No. 1, 1985, pp. 29–38.
doi:10.2514/3.22755

[19] Suder, K. L., Hathaway, M. D., Okiishi, T. K., Strazisar, A. J., and Adamczyk, J. J., "Measurements of the Unsteady Flow Field Within the Stator Row of a Transonic Axial-Flow Fan," NASA TM-88945, 1987.

[20] Peters, A., and Spakovszky, Z. S., "Rotor Interaction Noise in Counter-Rotating Propfan Propulsion Systems," *Journal of Turbomachinery*, Vol. 134, No. 1, Jan. 2012, Paper 011002.
doi:10.1115/1.4003223

[21] Lengani, D., Paradiso, B., Marn, A., and Göttlich, E., "Identification of Spinning Mode in the Unsteady Flow Field of a Low Pressure Turbine," *Journal of Turbomachinery*, Vol. 134, No. 5, Sept. 2012, Paper 051032.
doi:10.1115/1.4004875

[22] Rienstra, S. W., and Hirschberg, A., *Introduction to Acoustics*, Eindhoven Univ. of Technology, Eindhoven, The Netherlands, 2004, pp. 199–235, Chap. 7.

[23] Holste, F., and Neise, W., "Noise Source Identification in a Propfan Model by Means of Acoustical Near Field Measurements," *Journal of Sound and Vibration*, Vol. 203, No. 4, 1997, pp. 641–665.
doi:10.1006/jsvi.1996.0890

[24] Adamczyk, J. J., "Model Equation for Simulating Flows in Multistage Turbomachines," American Soc. of Mechanical Engineers Paper 1985-GT-226, 1985.

[25] He, L., "Fourier Methods for Turbomachinery Applications," *Progress in Aerospace Sciences*, Vol. 46, No. 8, 2010, pp. 329–341.
doi:10.1016/j.paerosci.2010.04.001

[26] Hubinka, J., Santner, C., Paradiso, B., Malzacher, F., Göttlich, E., and Heitmeir, F., "Design and Construction of a Two Shaft Test Turbine for Investigation of Mid Turbine Frame Flows," *19th International Symposium on Airbreathing Engines*, AIAA Paper 2009-1293, Sept. 2009.

[27] Hubinka, J., Paradiso, B., Santner, C., Göttlich, E., and Heitmeir, F., "Design and Operation of a Two Spool High Pressure Test Turbine Facility," *Proceedings of Ninth European Turbomachinery Conference*, March 2011, Paper 112.

[28] Persico, G., Gaetani, P., and Guardone, A., "Design and Analysis of New Concept Fast-Response Pressure Probes," *Measurement Science and Technology*, Vol. 16, July 2005, pp. 1741–1750.
doi:10.1088/0957-0233/16/9/005

[29] Mayrhofer, N., and Woisetschläger, J., "Frequency Analysis of Turbulent Compressible Flows by Laser Vibrometry," *Experiments in Fluids*, Vol. 31, No. 2, 2001, pp. 153–161.
doi:10.1007/s003480000268

[30] Hampel, B., and Woisetschläger, J., "Frequency- and Space-Resolved Measurement of Local Density Fluctuations in Air by Laser Vibrometry," *Measurement Science and Technology*, Vol. 17, No. 10, 2006, pp. 2835–2842.
doi:10.1088/0957-0233/17/10/039

[31] Hecht, E., *Optics*, 4th ed., Pearson Education, San Francisco, 2009, pp. 528–534.

[32] Hall, K. C., Thomas, J. P., and Clark, W. S., "Computation of Unsteady Nonlinear Flows in Cascades Using a Harmonic Balance Technique," *AIAA Journal*, Vol. 40, No. 5, 2002, pp. 879–886.
doi:10.2514/3.15137

[33] Candès, E. J., Romberg, J. K., and Tao, T., "Robust Uncertainty Principles: Exact Signal Reconstruction from Highly Incomplete Frequency Information," *IEEE Transactions on Information Theory*, Vol. 52, No. 2, 2006, pp. 489–509.
doi:10.1109/TIT.2005.862083

[34] Spataro, R., Santner, C., Lengani, D., and Göttlich, E., "On the Flow Evolution Through a LP Turbine with Wide-Chord Vanes in an S-Shaped Channel," *Proceedings of ASME Turbo Exposition 2012*, American Soc. of Mechanical Engineers Paper GT2012-68178, Fairfield, NJ, June 2012.

[35] ANSYS CFX-Solver Modeling Guide, Ansys, Ver. 13.0, Canonsburg, PA, 2010.

[36] Menter, F. R., "Two-Equation Eddy-Viscosity Turbulence Models for Engineering Applications," *AIAA Journal*, Vol. 32, No. 8, 1994, pp. 1598–1605.
doi:10.2514/3.12149

[37] Santner, C., Paradiso, B., Malzacher, F., Hoeger, M., Hubinka, J., and Göttlich, E., "Evolution of the Flow Through a Turning Mid Turbine Frame Applied Between a Transonic HP Turbine Stage and a Counter-Rotating LP Turbine," *Proceedings of Ninth European Turbomachinery Conference*, March 2011, Paper 110.

[38] McAlpine, A., and Fisher, M. J., "On the Prediction of "Buzz-Saw" Noise in Aero-Engine Inlet Ducts," *Journal of Sound and Vibration*, Vol. 248, No. 1, 2001, pp. 123–149.
doi:10.1006/jsvi.2001.3770

[39] Kielb, J. J., Abhari, R. S., and Dunn, M. G., "Experimental and Numerical Study of Forced Response in a Full-Scale Rotating Turbine," American Soc. of Mechanical Engineers Paper 2001-GT, Fairfield, NJ, 2001.

[40] Southworth, S., Dunn, M., Haldeman, C., Chen, J.-P., Heitland, G., and Liu, J., "Time-Accurate Predictions for a Fully Cooled High-Pressure Turbine Stage Part I: Comparison of Predictions with Data," *Journal of Turbomachinery*, Vol. 131, No. 3, 2009, Paper 031003.
doi:10.1115/1.2985075

[41] Green, B. R., Mathison, R. M., and Dunn, M. G., "Comparison of Harmonic and Time Marching Unsteady Computational Fluid Dynamics Solutions with Measurements for a Single-Stage High-Pressure Turbine," *Journal of Turbomachinery*, Vol. 136, No. 1, 2014, Paper 011005.

J. Bons
Associate Editor